Research Square

Preprints are preliminary reports that have not undergone peer review.
They should not be considered conclusive, used to inform clinical practice,
or referenced by the media as validated information.

Pendant drop rotation in vertical, turbulent, shearing flows

Jacob Douglas Dockery
University of Tennessee at Knoxville
Sagar Gharti
Embry–Riddle Aeronautical University
Michael Kinzel
Embry–Riddle Aeronautical University
Andrew Keith Dickerson
ad@utk.edu

University of Tennessee at Knoxville

Research Article

Keywords: pendant drop, oscillation, wind tunnel, turbulence

Posted Date: June 19th, 2026

DOI: https://doi.org/10.21203/rs.3.rs-9991013/v1

License: This work is licensed under a Creative Commons Attribution 4.0 International License.
Read Full License

Additional Declarations: No competing interests reported.

Pendant drop rotation in vertical, turbulent, shearing flows

Jacob D. Dockery[1], Sagar Gharti[2], Michael P. Kinzel[2], Andrew K. Dickerson[1]*

[1]Mechanical and Aerospace Engineering, University of Tennessee, Knoxville

[2]Aerospace Engineering, Embry-Riddle Aeronautical University, Daytona Beach

* Corresponding author: ad@utk.edu

June 10, 2026

Abstract

In natural and engineering applications, mobile drops frequently encounter nonuniform flows, and such interactions are both uncharacterized and difficult to experimentally observe. In this study, we record the dynamics of pendant drops, a natural and ubiquitous drop state, subject to the non-uniform disturbances of aerodynamic turbulence and shear. Our turbulent, shearing flow is formed by a pseudo-coaxial jet. By protruding a co-flowing jet through the center of a vertical, suction-type vertical wind tunnel, we create a novel flow field termed sheathed, coaxial jet-flow (SCJF). Tuning the jet (core) and tunnel (sheath) velocities allows us to create turbulent, shearing flow fields that arise from the interactions at the flow interface. We employ an Eulerian-based finite-volume CFD solver within Star-CCM to characterize our novel flow and understand the drop dynamics therein. Subject to turbulent, shearing flows, pendant drops may rotate. The onset of drop rotation is influenced by turbulence below a threshold Reynolds number defined by the needle diameter. We find that pendant drop dynamics in SCJF are influenced by the size of the capillary support, the velocity ratio between the core and sheath, the drop size, and the magnitudes of turbulence intensity and shear imposed on the drop. We find that pendant drops exhibit limited modal behavior compared to that observed for laminar conditions and that small drops rotate faster than large drops. We form a scaling argument based upon the energetics of a rotating drop to reveal that dimensionless drop rotation, given by a modified Strouhal number, scales with an inverse drop Reynolds number. By comparing our results to the findings of our previous work in laminar flows, we discover that turbulence does not notably influence dimensionless drop rotation.

Keywords: [pendant drop, oscillation, wind tunnel, turbulence]

1 Introduction

Drops suspended from needles, pendant drops, have received much attention in recent decades due to their suite of applications. Understanding the dynamics of pendant drops is crucial for environmental studies[14,20], lab-on-a-chip devices[45], ink-jet printing[40], pharmaceutics[17,32], and surface tension measurements[26]. Additionally, pendant drops provide a convenient platform by which to characterize the interaction of drops with aerosols[33], gaseous species[18], and flow structures[8]. Continuous attachment to the capillary allows pendant drops to be enlarged[21], retracted[43], released[15,44], charged[11], and held in steady view[21] whilst subject to a wide range of conditions. Phenomena surrounding pendant drops, such as their natural frequency[27], shape perturbations[4], rotational dynamics[8,21], jetting transition[7], stability[46], and pinch-off[36], have been characterized for ambient and uniform conditions, but the dynamics of pendant drops in response to more dynamic external perturbations is considerably less explored. Investigations concerning pendant drop dynamics in response to external disturbances have been limited to uniform disturbances such as laminar flows[8,21], acoustic waves[6], and movement of the capillary support[41], with no attention diverted to pendant drop dynamics

in response to more dynamic, inharmonic disturbances. In this study, we subject pendant drops to the non-uniform disturbances of turbulent, shearing flow and record their dynamics as shown in **Fig.1**a.

Exposed to external forces, pendant drops deform, rotate, and shear. In acoustic fields, pendant drops exhibit longitudinal, translational, and rotational modes[25]. The resonance frequency at which pendant drops experience longitudinal and rotational modes is a function of drop size, in which increasing drop size decreases the resonant frequency[25]. In ascending laminar flows parallel with gravity and the supporting needle, pendant drops rotate and experience deformation quantified by a variety of behavioral modes[8,21]. In our previous study with ascending laminar flows, pendant drop rotation was shown to be influenced by wind speed, needle diameter, drop diameter, wettability of the straight-cut needle, and liquid surface tension[8]. Shape deformation was shown to coincide with small rotational amplitudes compared to the needle[8]. Through experiment and modeling, Lee and Hwang showed that pendant drop dynamics and equilibrium shapes at a fixed velocity are influenced by the longitudinal length of the pendant drop, the distance from the tip of the needle to the drop apex[21]. They highlight the existence of critical longitudinal drop lengths that denote regions of stability and instability for a fixed windspeed based upon the variation of the tilting angle of the drop. Lacking in the study of pendant drop response to external perturbation is the drop response to more dynamic, less uniform excitation.

Raindrops, a close relative to hanging drops, have been characterized in response to both uniform and non-uniform disturbances. Falling through the atmosphere, raindrops are subject to both laminar (uniform) and turbulent (nonuniform) flows, in which they experience shape deformation[34], breakup[10], coalescence[37], and oscillations[35]. Turbulence augments drop canting angle, axis ratio, fall speed, and drop oscillation compared to that which would occur in laminar conditions[47]. Similarly stated, non-uniform disturbances augment the drop response from those observed from uniform disturbances of the same medium. Subsequently, we expect the pierced counterparts of levitating drops to show augmented behavior from that observed in laminar flow. In this study, we subject pendant drops to a shearing, turbulent flow. The sheared, turbulent flow is

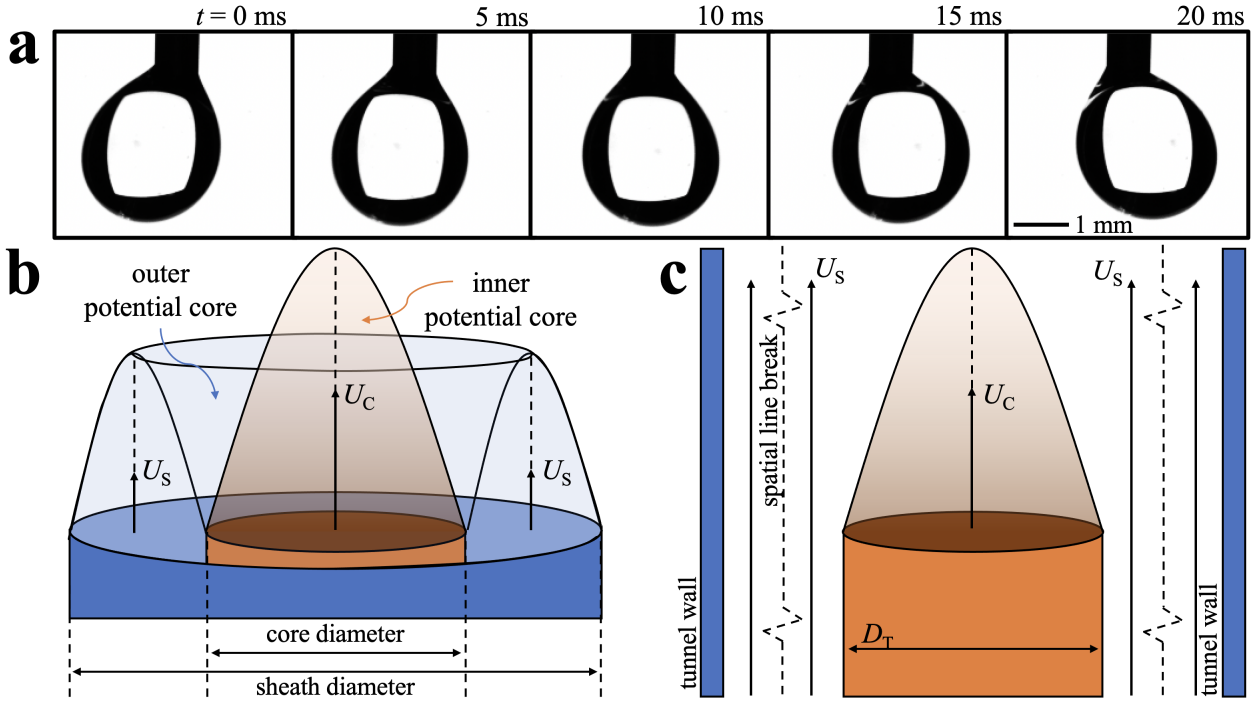


Figure 1: Pendant drops may oscillate when exposed to turbulent, shearing flow. **(a)** Time schematic of a drop of diameter 2.5 mm rotating 15.9 cm above the coaxial jet with a velocity of 4 m/s and a sheath flow velocity of 0.8 m/s. Our shearing, turbulent flow is created by sheathed, coaxial jet-flow, which is similar to a coaxial jet shown in **(b)**. By allowing a core jet to protrude and exhaust into a vertical wind tunnel, we create a sheathed, coaxial jet-flow shown in **(c)**.

created by the interaction between a core jet and a co-flowing sheathing airstream: a novel flow field that

we have coined the sheathed coaxial jet-flow (SCJF). Our SCJF is similar to a coaxial jet. Coaxial jets are characterized by a core jet that is encircled by a sheath jet[38]. Coaxial jet characteristics are well described by the interaction between two potential core flows, schematized in **Fig.1**b. The velocity ratio between the core and jet r_U, the diameter ratio r_D, and the outright core U_C and sheath U_S velocities influence conditions downstream of the outlet[38]. Shear between the core, sheath, and ambient surroundings leads to turbulence, vorticity, and breakdown of the potential cores[39]. Even when $r_U = 1$, the lip-thickness between the two flows gives rise to wake-like instabilities downstream[2]. The influence of the sheath flow upon the inner potential core length is given by e, which stands as the ratio between the potential core length with and without a sheath flow present[3]. Generally, when $r_U < 1$, the inner potential core is lengthened by the presence of the sheath flow. When $r_U > 1$, e falls below unity once r_U is sufficiently large and e is greatly influenced by r_D[38]. Downstream of the inner core breakdown, the two flows continue to mix and merge until the flow becomes fully developed. Once the flows have merged, there is a distance from the jet outlet at which the flow profile matches that of a singular jet[19].

We create our sheathed, coaxial jet flow by allowing the core flow to exhaust into the sheath flow, rather than having both the core and sheath jet into ambient conditions. By augmenting the physical dimensions of a coaxial jet, we create our shearing, turbulent flow. We radially expand the sheath diameter of the coaxial jet in **Fig.1**b and offset the plane of the core jet exits from that of the sheath to create our sheathed, coaxial jet flow, schematized in **Fig.1**c. In our case, the sheath flow boundary is the wall of the vertical wind tunnel, and the core jet is provided by a thin-walled tube protruding through the tunnel. We employ a computational model to characterize our novel flow and to provide numerical values for downstream conditions such as turbulent intensity and a velocity field. Additionally, we physically suspend drops at different heights above the core jet exit and record pendant drop motion in response to the aerodynamic, non-uniform disturbance.

2 Methods

2.1 Experimental Setup

In this study, we investigate the oscillatory behavior of pendant drops exposed to sheath flow. The pull-type vertical wind tunnel from Dockery *et al.* 2024, was augmented to allow for the interaction of a core and sheath flow and equipped with a secondary 8" duct fan. The augmented vertical wind tunnel is shown in **Fig.2**. More details concerning the tunnel dimensions can be found in our previous article[8]. The sheath flow, induced by a dual fan system, is controlled with an ITech IT-M7721L variable AC power supply and 2000 VA (Volt-Amperes) secondary voltage regulator. Sheath flow velocity U_S is measured using a TSI Velocicalc anemometer with 0.01-m/s precision. The core flow is supplied by a $D_T = 1.27$-cm diameter brass tube with a 0.56-cm wall thickness. The tube penetrates the HEPA filter, honeycomb laminarizers, and contraction section such that its position is viewable and controllable within the observation section. The core flow is supplied by the flow diagram depicted in **Fig.2**b. The core flow velocity U_C is measured using a TSI model 4043 flow meter. Centered above the tube exit, a drop of diameter D is extruded onto a needle of diameter D_N using a New Era NE-800 syringe pump as shown in **Fig.2**c. Pendant drop motion is backlit, then captured at 1000 fps using a Photron Nova S6 high-speed camera attached with a 105 mm 1:2.8 Sigma lens. We record drop rotation at 3 heights above the tube outlet L1 = 2 cm, L2 = 16 cm, and L3 = 32 cm. Drops at each location are subject to velocity fields characterized by $r_U = 0.2$,0.4,...,1.4 and $U_S = 2, 4$ m/s, except at L3 where $r_U = 0.2, 0.4$ are untested for $D_N = 0.08$ cm.

Videos of drop motion are binarized and analyzed using bespoke code in MATLAB. Using the needle as a physical scale, we track the drop centroid x_0, drop volume V_D, vertical distance from the tube exit to needle d, and angular velocity ω. The drop angular velocity is calculated by tracking the lateral position of x_0 and is averaged across a minimum of 1.5 periods.

2.2 Computational approach for characterizing tunnel conditions

We employ Star-CCM+ to characterize the flow delivered to the pendant drop at test locations in the tunnel. An Eulerian-based finite-volume CFD solver is used to provide pressure and velocity fields. Conservation of mass and the Navier-Stokes equations are solved simultaneously in axisymmetric cylindrical coordinates using a finite-volume discretization, where the geometric source terms arising from axisymmetry are automatically

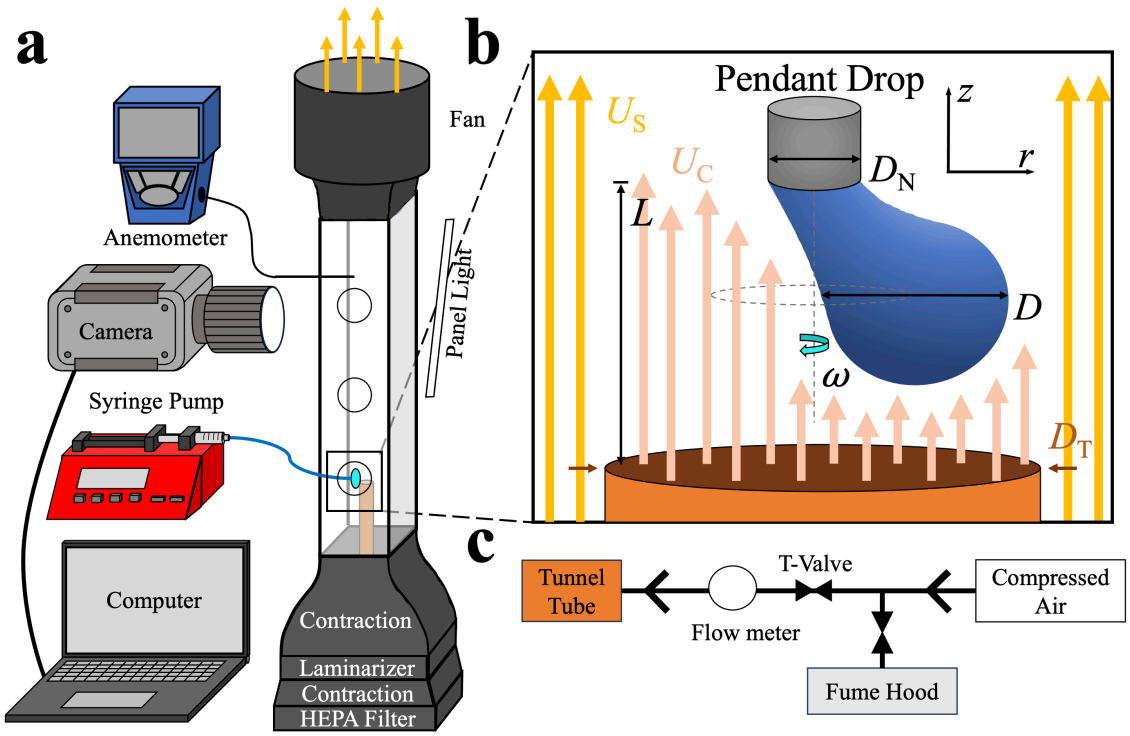


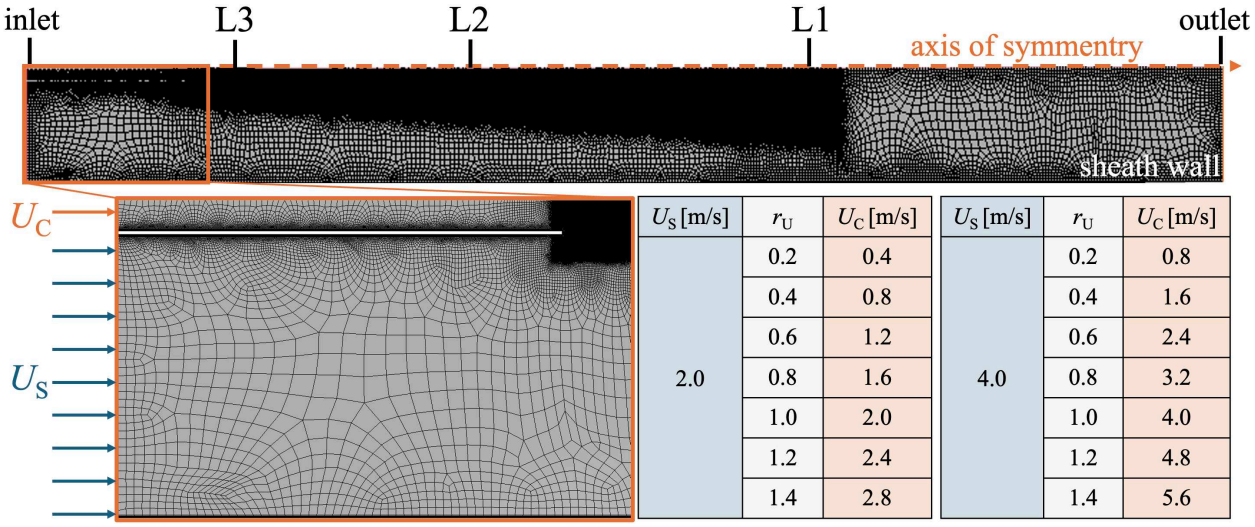
Figure 2: Schematic of experimental setup displaying pertinent dimensions and flow system. (**a**) Vertical wind tunnel wherein drop oscillation in sheath flow is investigated. (**b**) Zoom square depicting pertinent dimensions of a pendant drop, core and sheath flow. (**c**) Pictorial diagram of the system used to deliver laminarizer core flow.

accounted for by the STAR-CCM+ solver. The simulations are executed using a steady-state, segregated, pressure-based solver. The SIMPLE algorithm[28] is employed for pressure-velocity coupling, and second-order spatial discretization schemes are used for the momentum equation to ensure adequate accuracy. Convergence is assessed by monitoring the residual levels for continuity, momentum, turbulent kinetic energy, and specific dissipation rate, with a convergence criterion of 10^{-5} for all scaled residuals. Air is modeled as an incompressible, Newtonian fluid with a density of $\rho_a = 1.27$ kg/m^3 and a dynamic viscosity of $\mu_a = 1.8 \times 10^{-5}$ Pa $\cdot$ s. Turbulence is represented using the k–ω SST model developed by Menter[24], which blends the k–ω formulation near the solid walls with the k–ε model in the freestream. This blended formulation makes the SST model well-suited to this problem, providing accurate resolution of the shear layer at the core-sheath interface while maintaining robustness under the adverse pressure gradients present near the jet exit region.

The axisymmetric computational domain developed to simulate the flow is shown in **Fig.3**. A 2-D axisymmetric formulation is adopted to reduce computational cost while preserving accuracy in the quantities of interest. The coaxial jet and core tube are rotationally symmetric by design; the primary geometric departure from axisymmetry is the square cross-section of the sheath duct (12 cm $\times$ 12 cm). This is addressed using the hydraulic diameter, $D_h = 4A/P = 0.12$ m, where A is the duct cross-sectional area and P is the wetted perimeter. For a square duct, D_h equals the side length, so the axisymmetric domain is assigned an outer radius of $D_h/2 = 6$ cm, preserving the hydraulic diameter of the square duct. This equivalence is a standard approximation for turbulent duct flows, where corner-driven secondary velocities are weak (typically less than 1–2% of the bulk velocity[12]) and the velocity profile approaches axisymmetry well away from the duct corners, as confirmed by the direct numerical simulation of turbulent square-duct flow[12]. Since the pendant drop is located on the tunnel centerline, far from the square walls, the influence of corner geometry on the quantities of interest is negligible.

The core and sheath inlets are modeled using velocity inlet boundary conditions, while the outlet is set as a pressure outlet with a gauge pressure of 0 Pa. All solid walls are treated as no-slip surfaces, and the axis of symmetry is applied along the centerline. Inlet velocities for the core and sheath are specified for

each case as summarized in **Fig.3**. The domain is discretized using a structured quadrilateral mesh with prism layers near solid boundaries to resolve velocity gradients. The prism layer comprises 15 layers with a first cell height of 0.05 mm, yielding wall y^+ values in the range 0.10 to 1.62 across all cells, which is consistent with the All-wall-y^+ near-wall treatment model. Local refinement is applied near the jet exit region to accurately capture shear-layer development. We include details of a mesh sensitivity study and a grid convergence index analysis in the Supplement.



U_S [m/s]	r_U	U_C [m/s]
2.0	0.2	0.4
	0.4	0.8
	0.6	1.2
	0.8	1.6
	1.0	2.0
	1.2	2.4
	1.4	2.8

U_S [m/s]	r_U	U_C [m/s]
4.0	0.2	0.8
	0.4	1.6
	0.6	2.4
	0.8	3.2
	1.0	4.0
	1.2	4.8
	1.4	5.6

Figure 3: Computational domain, mesh, and boundary conditions used for the CFD simulations.

Turbulence at the core and sheath inlets is initialized using a turbulence intensity of 1% and a turbulent viscosity ratio of 10, which are common for low free-stream turbulence cases. The sheath flow undergoes successive conditioning before reaching the observation section: it first passes through a HEPA filter, which acts as a high-resistance porous screen analogous to the damping screens shown to suppress turbulent fluctuations by Dryden and Schubauer[9]; then through a contraction section; then through a honeycomb laminarizer, which further inhibits lateral velocity components[22]; and finally through a second contraction section. Each contraction further attenuates the residual axial turbulence intensity. Longitudinal turbulent fluctuations tend to scale approximately as $1/C$, where C is the contraction ratio, as originally proposed by Prandtl[29] and later derived theoretically by Batchelor and Proudman[5] via rapid distortion theory. The cumulative effect of this conditioning stack, filter, contraction, honeycomb, contraction, makes a low inlet turbulence intensity of 1% a physically conservative estimate for the sheath flow at the CFD inlet boundary.

3 Results

3.1 Sheathed coaxial jet-flow produces a turbulent-shearing flow

Using the computational methods described in Section 2.2, we calculate the local variation of velocity U and turbulence intensity I for the experimental volume, shown in **Fig.4**. For each r_U at L3, we observe the effects of the boundary layer formed on the inside and outside of the tube wall as seen in **Fig.4**c,f,i,l. Turbulence generated within the boundary layers within and external tube wall is the main source of turbulence at L3. Downstream of L3, the boundary layer dissipates and shear is the dominant source of turbulence, as shown in **Fig.4**. The value of r_U dictates the magnitude of shear at the core-sheath interface. When $r_U < 1$, the sheath shears the core flow, consequently accelerating the core to a speed similar to the sheath. When $r_U = 1$, no shear occurs between the core and sheath. Thus, the boundary layer alone is responsible for any turbulence and vortical formation downstream. When $r_U > 1$, the core flow shears the sheath flow and thus accelerates the sheath.

The velocity and turbulence at a given height are not isotropic in the transverse direction. Thus, the magnitude of U and I that a pendant drop experiences is influenced by drop size. We plot the streamwise

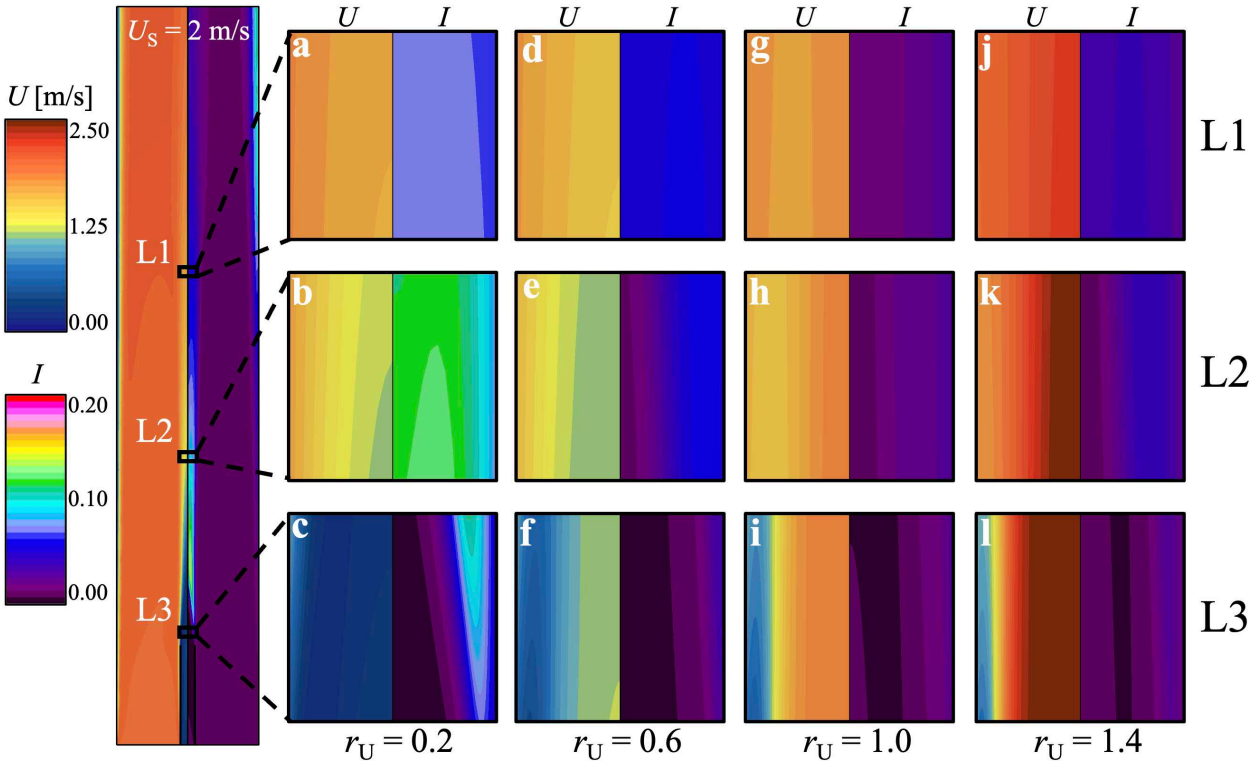


Figure 4: Plots of CFD predictions of local variation of U and I for $U_S = 2$ m/s, and $r_U = 0.2$, 0.6, 1.0, and 1.4 at L1, L2 and L3. We show the large-scale simulation on the left-hand side for $U_S = 2$ m/s and $r_U = 0.2$. We plot the local variation of U and I at the three regions at which pendant drops are placed for $r_U = 0.2, 0.6, 1.0,$ and 1.4 in **a-l**. The bounds of these regions are given by $1.2D_T \times 1.2D_T$, and serve as boundaries by which to calculate averaged values of U and I.

velocity profile and turbulence intensity profile in the transverse direction in **Fig.5** for $r_U = 1.4, 1.0,$ and 0.6 at each fixture position. The boundary layer within the core flow gives the velocity profiles a shape characteristic of Poiseuille flow near L3 as seen in **Fig.5**a-c. Associated with this boundary layer, there exist high levels of turbulence near the tube wall as shown in **Fig.5**d-e. Downstream of L3, we observe the dissipation of the turbulent boundary layer as the slope of the velocity profile decreases as L increases, as shown in **Fig.5**a-c. Turbulence generally increases downstream of the tube outlet as evidenced by the peaks of **Fig.5**d-f. Shear at the flow interface gives rise to turbulence above the tube wall, and turbulence spreads radially from the interface as L increases, as shown by **Fig.5**d-f.

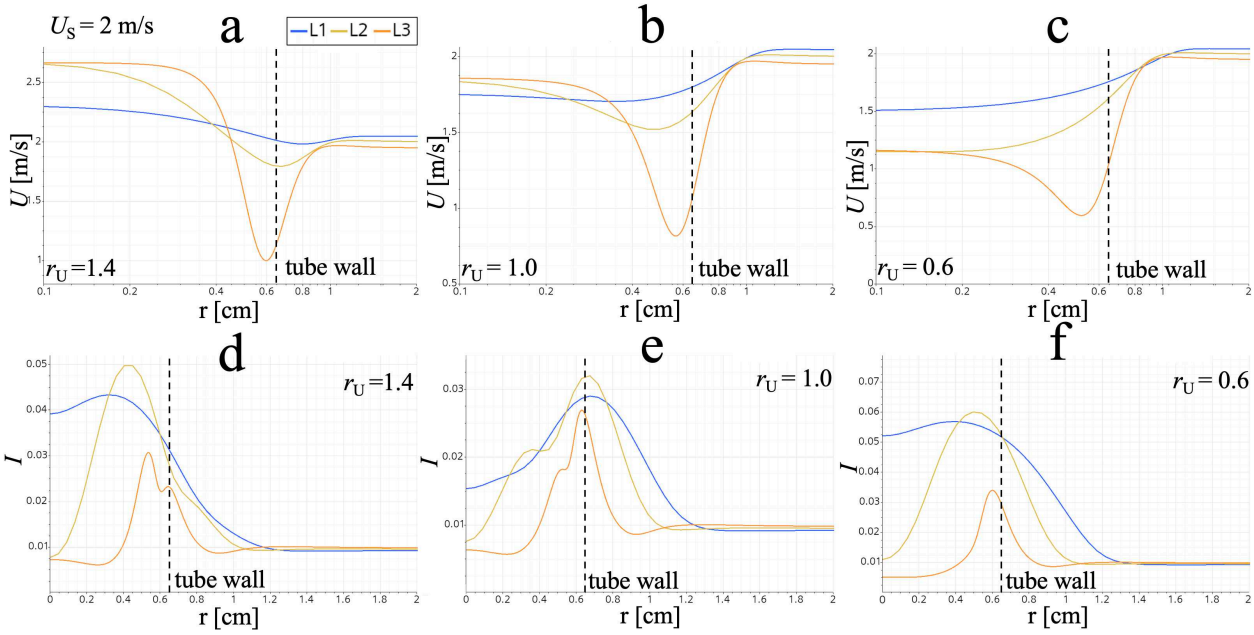


Figure 5: Plots of CFD predictions of the streamwise velocity profile in the transverse direction r are plotted for L1, L2, and L3 for $U_S = 2$ and $r_U = 1.4, 1.0,$ and1.6 in **a-c**. The corresponding magnitudes of turbulent intensity for **a-c** are plotted against streamwise position in **c-d**.

We take the average of local U and I for each flow condition and fixture position across the regional boundaries depicted in **Fig.4**a-l to form the mean velocity U_M and turbulent intensity I_M. We plot U_M and I_M for all flow conditions and fixture positions in **Fig.6**. We find that in general, as L increases U increases for $r_U \leq 1$ as seen in **Fig.6**a-b. When $r_U > 1$, the flow accelerates between L3 and L2, and experiences little change in U_M between L2 and L1. The acceleration between L3 and L2 is due to a slight expansion of the sheath flow, reducing the effective cross-sectional area of the core flow. When $r_U < 1$ flows are generally more turbulent than when $r_U \geq 1$, as shown in **Fig.6**c,d. There exists a minimum in I_M at $r_U = 1.0$, above which I_M increases with r_U. Thus, when shear is minimized, turbulence is also, and increasing shear increases turbulence. The average turbulence across r_U and U_S at each fixture position is 0.04, 0.043, and 0.016 at L1, L2, and L3 respectively. Thus, we find that L2 is the most turbulent location, though only marginally. For $r_U < 0.6$, L2 is far more turbulent than both L1 and L3.

3.2 Modal behaviors are simplified in turbulent-shearing flow

We perform $N = 550$ trials of pendant drops consisting of 34 flow conditions for drops $D = 0.981 - 9.6$ mm in diameter, suspended from $D_N = 0.8$-mm and 1.8-mm diameter needles, and placed at three distances from the tube outlet. For fixed inlet conditions (constant U_S and U_C), changing the drop fixture elevation varies the amount of turbulence and drag the drop experiences. We record drop rotational frequency ω and amplitude χ for hanging drops in sheathed, coaxial jet-flow. The dynamics of the drops in this study are best interpreted in the context of pendant drop dynamics in laminar airflow.

In response to laminar airflow, we found that pendant drops exhibit seven behavioral modes characterized

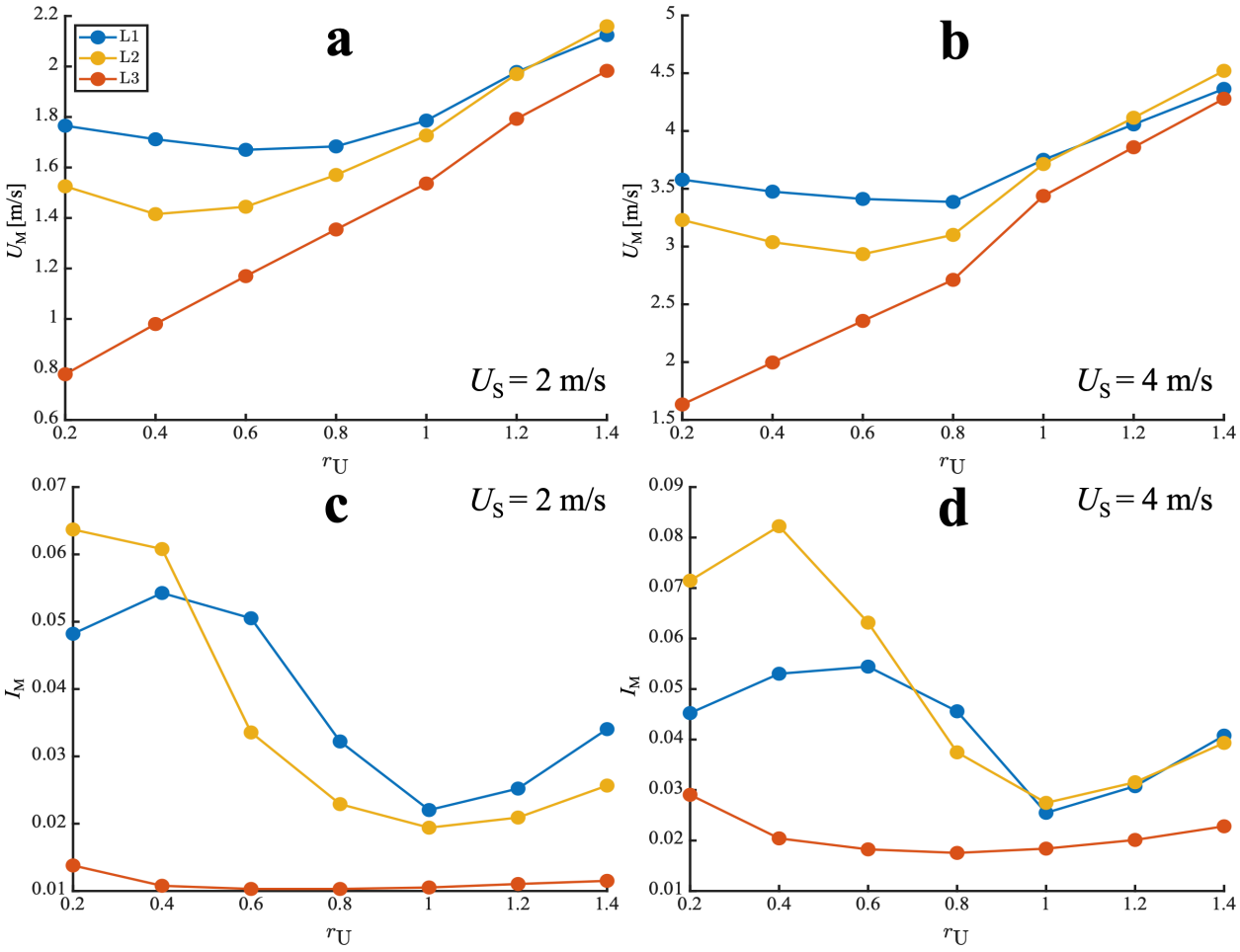


Figure 6: Variation of CFD prediction of the average velocity magnitude U_M (**a-b**) and turbulence intensity I_M (**c-d**) across velocity ratio r_U for $U_S = 2, 4$ m/s at each fixture position.

by shape deformation and rotation[8]. Rotating drops were observed to rotate about an axis of rotation that was either static or dynamic. Drops rotating about a static axis parallel to the needle have little to no vertical oscillation as they rotate about the needle, contrasting the vertical oscillation of drops that rotate about a dynamic axis[8]. The metric for determining whether a drop has a static or dynamic axis of rotation is given by $y_0 P > A$, where y_0, P, and A are the vertical oscillation amplitude, perimeter, and cross-sectional area, respectively. When $y_0 P > A$, a dynamic axis of rotation exists[8]. Otherwise, the drop rotates about a static axis or does not rotate. Pendant drop shape deformation was determined by tracking the temporal ratio R_M/R_m and measuring its frequency Γ, the shape deformation frequency. R_M and R_m are the maximum and minimum distances from the drop centroid to the drop boundary[8]. Since Γ is influenced by drop rotation, we form a dimensionless parameter $\Omega = 2\pi\Gamma/\omega$, the shape deformation factor, useful for describing the magnitude of shape deformation. In our previous work[8], a binary codex was employed to describe the rotation and deformation dynamics of the drops, (α, β). Rotation and rotational axis characteristics are described by α and the magnitude of shape deformation is given by β. For $\alpha = 0$, 1a, and 1b, drops exhibit no rotation, rotation about a static axis, and rotation about a dynamic axis, respectively. For $\beta = 0$, 1a, and 1b, drops exhibit no shape deformation, $1.85 < \Omega < 2.15$, low frequency shape deformation $1.85 > \cup\ 2.15 \leq \Omega < 5$, and high frequency deformation $\Omega \geq 5$, respectively. We employ this same binary codex to describe the behaviors of pendant drops in sheathed, coaxial jet flow.

We display the most common behavioral modes across all needle fixture positions for one needle diameter and all r_U in **Fig.7a**. In general, the most common behavioral mode is (1a,0). Second to (1a,0), the most common mode observed for a given r_U is (1b,0). Depictions of these two modes are given in **Fig.7b**. Unlike

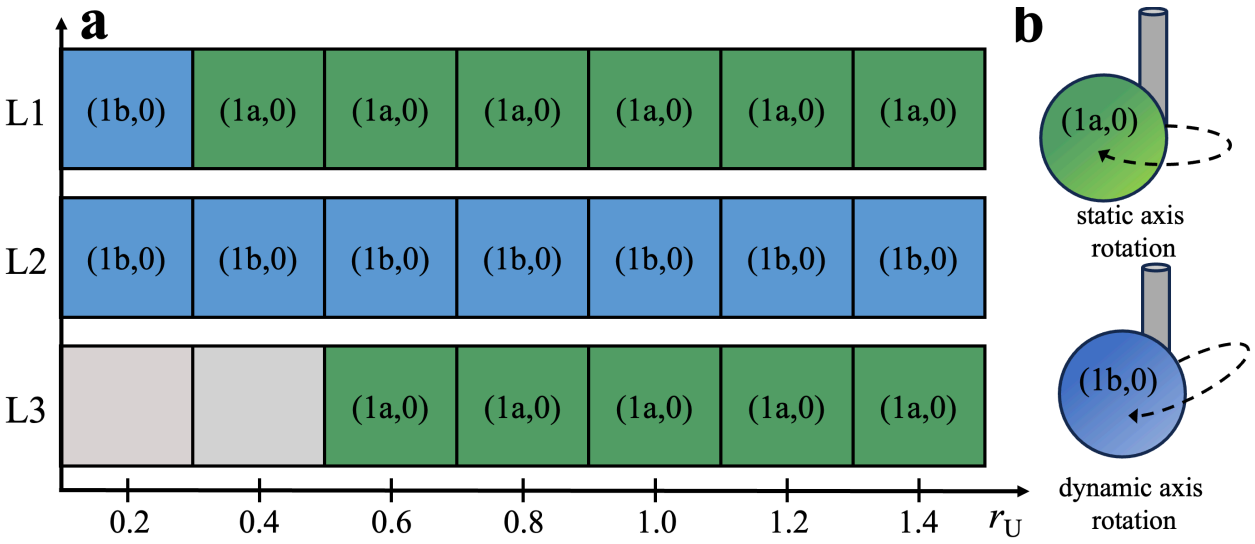


Figure 7: Pendant drops exposed to ascending, sheathed coaxial jet-flow rotate according to discrete behavioral modes. (**a**) The most common mode is shown for across r_U and levitation height for $D_N = 0.8$ mm. (**b**) Diagrams of the modes in **a** displaying rotation about static and dynamic axes.

drops in laminar flow, we do not observe prominent modes that are characterized by shape deformations. Simply stated, most pendant drops in sheathed coaxial jet flow do not deform as they rotate. We hypothesize that the lack of observed shape deformations in sheathed flow, compared to laminar flow, is due to the presence of turbulence.

3.3 Pendant drops rotate in turbulent-shearing flows

In the presence of shearing, turbulent flow (sheathed, coaxial jet-flow), pendant drops may oscillate and deform. The rotational behavior of hanging drops in laminar flow is best captured by the use of the Reynolds number. Since measuring the velocity at the drop location would alter the flow field, we employ the model described above (Section 2.2) to gather the mean velocity at the drop location U_M, and define $\mathrm{Re} = \rho_a U_M D/\mu_a$ to characterize the behavior of pendant drops in sheathed, coaxial jet-flow. Where ρ_a is air density, D is drop hydraulic diameter, and μ_a is the dynamic viscosity of air.

In our turbulent flow, pendant drops rotate at angular velocities $\omega = 2\pi f$ influenced by drop size, windspeed, needle diameter, and turbulent intensity. We plot ω vs Re for three fixture positions of drops adhered to the same needle of $D_N = 0.08$ cm in **Fig.8**a, providing 84 different near-field flows as a result of several combinations of U_S, U_C, and L. This plethora of experimental combinations encompasses a wide range of I_M and U_M for a wide range of drop sizes, and allows for a sweeping analysis of pendant drop rotation in our dynamic flow. In general, we find that increasing Re decreases ω, as shown in **Fig.8**a; where small drops rotate faster than large drops. While generally small drops rotate faster than large drops in sheathed coaxial jet-flow, the spread of the data across Re for each fixture position in **Fig.8**a implies that the law is slightly more complicated compared to laminar flow. We find that the efficacy of the Reynolds number to determine drop rotation depends on the magnitude turbulence that a drop experiences at that location. At L3, where the flow is predominantly laminar, Re does not predict ω. As turbulence increases, Re is a better predictor of drop rotation for a fixed needle size, which is evidenced by the collapse of data for L2 and L1, particularly L2, where turbulence is greatest (**Fig.6**c,d). Simply put, the onset of turbulence collapses rotation to be a function of Re only.

Given that Reynolds number characterizes wake behavior and dynamics of spheres[31] and tethered-spheres[13,42], it is not surprising that Re captures the dynamics of pendant drops. In our previous study, to illicit the effect of wake structure upon pendant drop dynamics in laminar flow, we adjusted the size of the needle support. Changing the size of the needle either greatly obstructs (large D_N) or slightly obstructs (small D_N) vortical formation in the rear of the drop. We hypothesized that changing the size of the needle

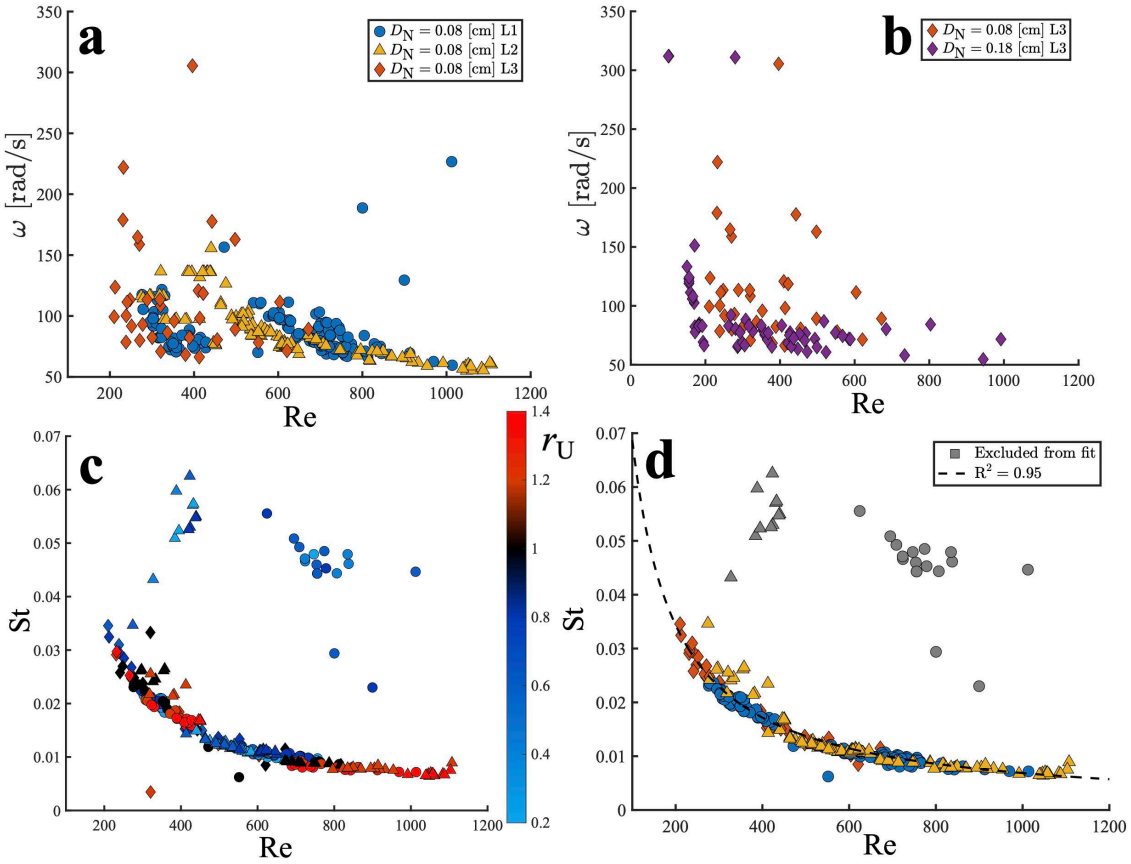


Figure 8: The rotational dynamics of pendant drops in ascending, sheathed coaxial jet flow are influenced by drop size, core flow velocity, distance from the jet outlet, and the diameter of the needle support. Plot of (**a**) ω vs Re for one needle at L1, L2, and L3 and (**b**) for two needles at L3. (**c**) Re vs St for $D_N = 0.08$ cm and all L, with blue, black, and red points corresponding to $r_U < 1, r_U = 1,$ and $r_U > 1$, respectively. (**d**) St $\sim$ Re^{-1} is plotted with gray points excluded from the fit.

support in laminar flows influences ω due to wake interactions with the needle and the needle influence on drop shape[8]. We likewise expect needle size to affect drop dynamics in turbulent conditions. We plot ω vs Re for drops adhered to two different needles at L3 in **Fig.8**b. At similar Re, drops affixed to smaller needles rotate at a higher ω, a contrast to the dynamics of pendant drops in laminar flows, where drops adhered to larger needles rotate faster than those adhered to smaller needles[8]. The decreased rotation for drops affixed to large needles is likely due to a reduction of the coherent vortex shedding behind the drops, influenced by the growing turbulent boundary layer formed at the interface of the core and sheath flow near the tube outlet.

We gain a clearer picture of how rotation varies with airspeed by employing a modified Strouhal number $\mathrm{St} = fD/U_\mathrm{M}$ that captures the efficacy of a pendant drop to convert the kinetic energy of the ascending airflow to rotation. We plot St vs Re according to fixture position and r_U in **Fig.8**c for the data in **Fig.8**a. In general, we find that St decreases with increasing Re across r_U and L. This trend indicates that turbulence intensity and shear profile, both of which vary according to L, r_U, and U_S (Section 3.1), do not generally augment dimensionless drop rotation. In laminar flows[8], St was also found to decrease with Re. The relationship between Re and St across disparate flows indicates that rotation is generally governed by Re and not so much influenced by the incoming flow profile. However, the efficacy of Re to fully characterize dimensionless rotation erodes for two sets of outlying data points above the main trend in **Fig.8**c; these points are at L1 and L2 for some subset of drop diameters in $U_\mathrm{S} = 2,\ 4$ m/s and for $r_\mathrm{U} < 1$. Thus, for flows characterized by a faster sheath and a slower core, there exists a critical drop size at which St dramatically increases. The observed increase in St is not due to an increase in rotation, but an increase in D for a fixed ω, which is discussed further below. It is worth noting that mathematically, St vs Re reduces to f vs U_M^2.

Changes to pendant drop shape alter drop-flow interactions, which affect rotation through changes in drag coefficient, wake formation, and ℓ. In quiescent conditions, hydrostatic and Laplace pressures compete to form the pendant drop shape. Introducing airflow to the pendant drop, aerodynamic pressure oblately deforms the drop. Changes in D_N/D alter pendant drop shape by changing the length of the three-phase contact line, changing drop curvature, particularly at the neck. Curvature governs the Laplace pressure and thus resistance to deformation. It follows that drops adhered to small needles are more resistant to aerodynamic flattening than drops adhered to large needles, which is consistent with our observations[8]. When D_N is held constant, increasing drop diameter weakens the Laplace pressure; subsequently making large drops less resistant to deformation and perturbation. To characterize the influence of modified drop shape upon rotation and to capture drop resistance to perturbation as a function of drop size, needle size, and windspeed, we define pendant drop shape parameter ϵ as a ratio of Laplace pressure($\sim \sigma/D$) to aerodynamic pressure ($\sim \rho_\mathrm{a} U^2$), scaled by D_N/D yielding

$$\epsilon \sim \frac{\sigma D_\mathrm{N}/D^2}{\rho_\mathrm{a} U_\mathrm{M}^2}. \tag{1}$$

Eq.(1) can be interpreted as a pressure ratio between aerodynamic pressure and a sustaining pressure. We define the sustaining pressure as the capillary force ($\sim \sigma D_\mathrm{N}$) acting over the projected drop area to the ascending flow ($\sim D^2$). The aerodynamic pressure deforms drop shape and drives rotation; whereas the sustaining pressure tethers the drop to the needle throughout rotation. Eq.(1) can be rearranged as $\epsilon \sim \mathrm{We}^{-1}(D_\mathrm{N}/D)$, where $\mathrm{We} = \rho_\mathrm{a} U_\mathrm{M}^2 D/\sigma$ is the Weber number. Physically, smaller ϵ values correspond to resistance to initial, rotation-inducing perturbations and promotion of oblateness. Accounting for influence of drop shape upon rotation, we define aerodynamic, lateral torque torque as $\tau_\mathrm{a} \sim \rho_\mathrm{a} U_\mathrm{M}^2 D^2 \ell \epsilon$. Since $\ell \sim D$, our expression for torque reduces to

$$\tau_\mathrm{a} \sim \rho_\mathrm{a} U_\mathrm{M}^2 D^3 \epsilon. \tag{2}$$

The rotation rate of pendant drops can be predicted by examining the energetics of the drop-flow system. The rotational power $P_\mathrm{a} \sim \tau_\mathrm{a}\omega$ acting upon the drop is damped by the rate viscous dissipation within the drop $\dot{\Phi}$. Viscous dissipation within an oscillating drop[1] is scales with $\dot{\Phi} \sim \mu_\mathrm{w} \int_V \dot{\mathbf{E}} : \dot{\mathbf{E}} \mathrm{d}V$, where $\dot{\mathbf{E}}$ is the strain rate tensor, μ_w is the viscosity of water, and V is volume. For a rotating pendant drop $\dot{\mathbf{E}} \sim \omega$, thus $\dot{\Phi} \sim \mu_\mathrm{w} D^3 \omega^2$. For steady rotation, $P_\mathrm{a} \sim \dot{\Phi}$, or,

$$\rho_\mathrm{a} U_\mathrm{M}^2 D^3 \epsilon \omega \sim \mu_\mathrm{w} D^3 \omega^2. \tag{3}$$

Eq.(3) reduces to $\rho_a U_M^2 \epsilon \sim \mu_w \omega$. Substituting Eq.(1) into Eq.(3) yields $\rho_a U_M^2 D_N \sigma \sim \mu_w \omega \rho_a U_M^2 D^2$. Solving for ω and eliminating like terms gives $\omega \sim D_N \sigma / (\mu_w D^2)$. Absorbing constants in our experiments into the scaling prefactor gives $\omega \sim D_N / D^2$. On a single needle (constant D_N),

$$\omega \sim \frac{1}{D^2}, \tag{4}$$

a result consistent with our previous work in laminar flow. The absence of U_M in our scaling law suggests that drop rotation is primarily a function of drop size and less dependent upon U_M.

We recast Eq.(3) to write,

$$\mathrm{St} \sim \mathrm{Re}^{-1}, \tag{5}$$

matching the trend in **Fig.8**c. We re-plot the data of **Fig.8**c in **Fig.8**d, where gray points corresponding to outlying sheath-dominated flows ($r_U < 1$) and non-gray points are colored according to fixture position. We fit the non-gray data with Eq.(5) yielding a correlation coefficient $R^2 = 0.95$. In some flows in which $r_U < 1$ and fixture position is fixed, rotating drops follow follow the prediction of Eq.(5) until a threshold Re is reached. However, since rotation is primarily driven by D, Eq.(4), it seems more likely that the deviation from the trend line corresponds to a critical D rather than a critical Re. We posit that the magnitude of this critical D is influenced by the increased shear at the interface between the core and sheath flow. To test this notion, we normalize D by tube diameter D_T and compare against St. We plot St vs D/D_T in **Fig.9**a,b for drops located at the two most turbulent fixture positions, L1 and L2. Generally, across both fixture positions and U_S, St decreases with increasing drop size below $D/D_T \approx 0.25$; which is a trend that aligns with our dimensionless scaling law $\mathrm{St} \sim \mathrm{Re}^{-1}$. Above $D/D_T \approx 0.25$, St drastically increases and subsequently deviates from the dominating trend of **Fig.8**d. Such deviation in pendant drop behavior shows that $D/D_T \approx 0.25$ bisects drop behavior into that which follows Eq.(5) and that which does not. After the initial rise in St when $D/D_T \gtrsim 0.25$, St decreases at L1 and increases at L2 with increasing D. Generally, we observe that data in regions of nonconformity in **Fig.9**a,b are in under-sheathed flows $r_U < 1$; which are flows that have higher levels of turbulent intensity and shear. It is likely that deviation from the Eq.(5) is due to the increased magnitude of turbulence and shear a drop experiences as drop diameter grows as depicted in **Fig.9**c and verified by the local variation of velocity plots in **Fig.9**d. We hypothesize that the differences in behavior for $D/D_T \gtrsim 0.25$ between L1 and L2 are due to the increased turbulence and shear at L2 compared to L1.

Thus far, pendant drop response to dynamic, non-uniform disturbances has been reported without direct comparison to uniform disturbances. To observe the influence of turbulence to augment rotation dynamics from those observed in laminar flows, we plot St vs Re for the colored data points of **Fig.8**d and the data of our previous work and apply a line of best fit following $\mathrm{St} \sim \mathrm{Re}^{-1}$ in **Fig.10**. We find that across laminar and turbulent flows pendant drop behavior follows $\mathrm{St} \sim \mathrm{Re}^{-1}$ with $R^2 = 0.91$. The efficacy of the dimensionless scaling law to capture drop rotation across both laminar and turbulent flows, barring regions of increased shear, indicates that dimensionless drop rotation is driven by the Reynolds number. For the outliers of **Fig.8**d, we posit drop rotation is still driven by inertia, but the relationship between St and Re has changed due to the inversion of the velocity well.

3.4 Turbulence mitigates the onset of pendant drop rotation

In response to aerodynamic perturbation, pendant drops may or may not rotate. For drop rotation to ensue at a given flow condition, a sufficiently large drop must be extruded from the needle. For each combination of fixture position, r_U, D_N, and U_S, we increase drop size until drop rotation begins. We define the minimum drop diameter that will rotate at a given flow condition as D_{min}. We plot D_{min} for $D_N = 0.08$ cm against the Reynolds number formed by the needle diameter, $\mathrm{Re}_N = \rho_a U_M D_N / \mu_a$, in **Fig.11** and color data points according to turbulence intensity. We employ Re_N to provide a baseline flow characterization for a fixed characteristic length across multiple flow conditions and drop sizes. We observe a bifurcation of the data at $\mathrm{Re}_N \approx 135$. When $\mathrm{Re}_N \gtrsim 135$, I_M has no observable effect upon D_{min}. When $\mathrm{Re}_N \lesssim 135$, at similar Re_N the onset of drop rotation is mitigated by increased turbulence intensity. Equally stated, small drops exposed to similar U_M may rotate at low I_M but remain stagnant when I_M increases. Increasing the non-uniformity of the aerodynamic disturbance augments the onset of drop response.

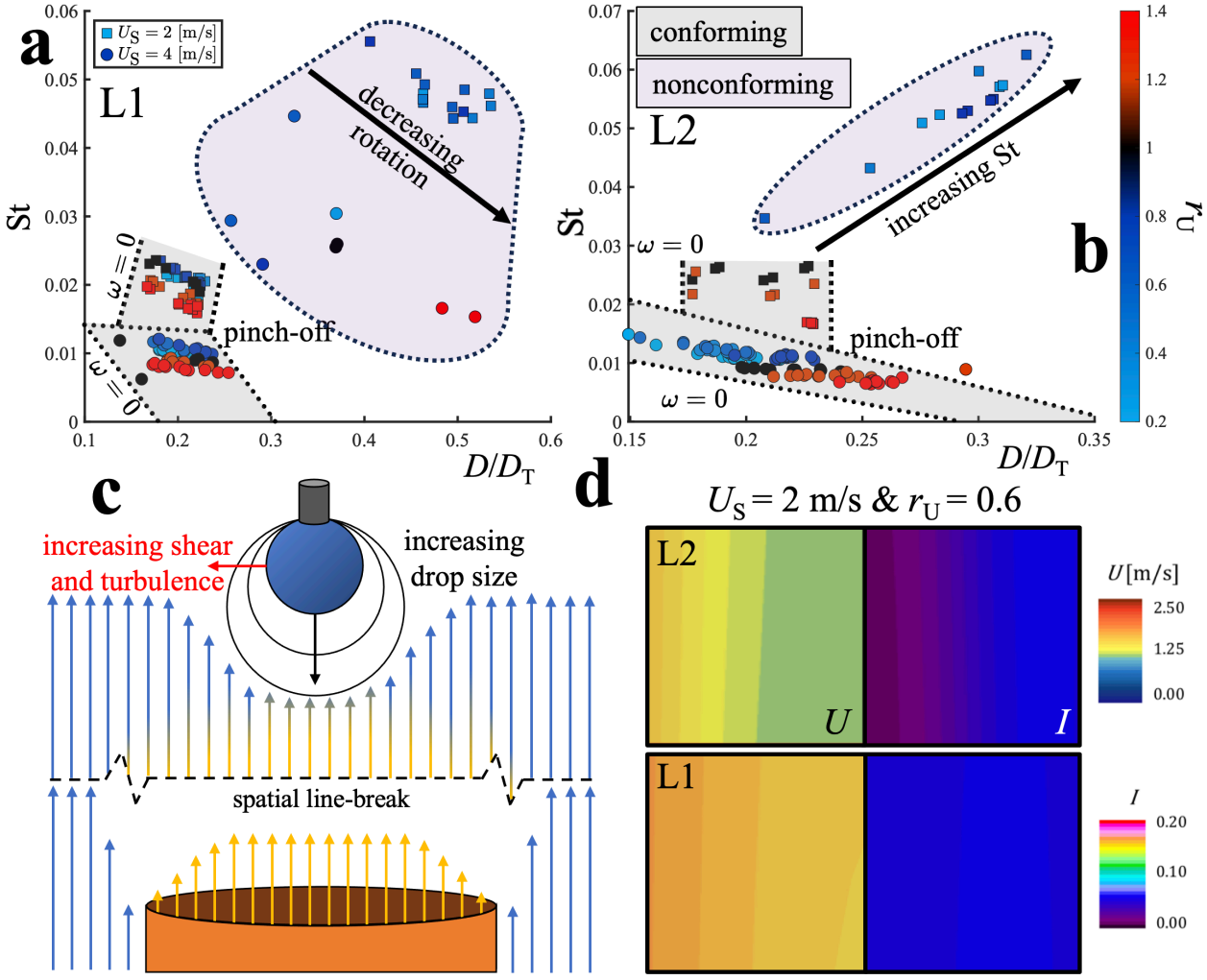


Figure 9: Plots of St vs Re at (**a**) L1 and (**b**) L2 for $U_S = 2, 4$ m/s with colors representing the magnitude of r_U. The colorbar in (b) corresponds to the data in (a) and (b). Data that conforms to the general trend are in gray regions, while regions of nonconformity are shaded purple. Dashed lines delineate behavioral boundaries in (a) and (b); where lines of black circles represent rotational onset and the critical drop size for $U_S = 2$ m/s and lines of black squares delineate the same for $U_S = 4$ m/s. (**c**) Pictorial depiction of the transverse velocity profile that a pendant drop experiences downstream of the tube. (**d**) Local variations of velocity taken from **Fig.4**e and **Fig.4**d that show that support the depiction in **c**.

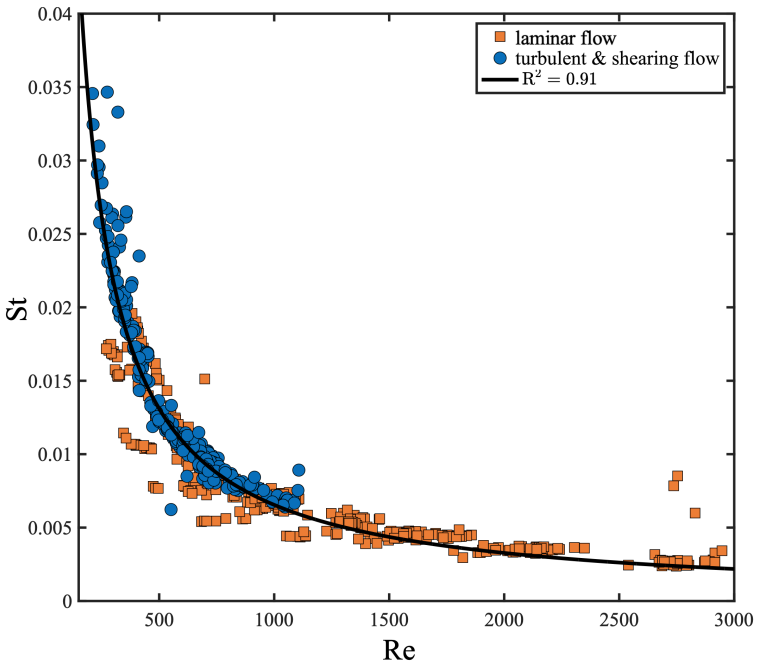


Figure 10: Dimensionless drop rotation is governed by Reynolds number across laminar and turbulent flows. We plot St vs Re for the colored data points of **Fig.8**d alongside the rotational data of pendant drops in laminar flows. We apply a line of best fit across both data sets following $\mathrm{St} \sim \mathrm{Re}^{-1}$.

The ability of turbulence to offset $D_{\min}$ offers insight into how drop rotation begins. In our previous work using laminar flows, we hypothesized that drop rotation arose as the result of vortex shedding[8]. In Lee and Hwang's investigation of pendant drop stability in vertical flows, they theorize that rotation arises as a result of a torque imbalance following small, natural instabilities[21]. When the drop sways slightly due to some instability, vertical-aerodynamic, gravitational, and surface tension torque compete to bring the drop back to rest below the needle or to thrust the tilted drop into rotational motion[21]. When restoring torques are greater than aerodynamic torque, the drop does not rotate[21]. Since increasing drag increases the likelihood that rotation will occur arising from an imbalance of torques, our finding that turbulence increases $D_{\min}$ is surprising. At $\mathrm{Re} < 1000$, low level turbulence intensity ($< 10\%$) has been shown to increase drag upon spheres[16,30] and to modulate vortical formation[30]. Therefore, increasing I_{M} enlarges aerodynamic torque, which should increase the likelihood of drop rotation. However, we have observed that increasing I_{M} at similar $\mathrm{Re_N} \lesssim 135$ cessates drop rotation. Given the apparent contradiction between the findings of our previous work[8], the work of Lee and Hwang[21], and our present work, the story surrounding the onset of pendant drop rotation is incomplete. Rather than drop rotation arising solely from vortical formation or a torque imbalance, drop rotation may likely arise out of the effectual combination of those phenomena. If the onset of rotation is influenced by vortical formation, then for a fixed $\mathrm{Re_N}$ and I_{M}, a sufficiently large drop size is required to invoke vortical formation that overcomes the turbulence structure about the drop.

4 Discussion

4.1 Influences upon drop behavior

The size of pendant drops in this study ranged from $D = 0.98 - 9.6$ mm, a range truncated by pinch-off for our select combinations of r_{U} and U_{S}. We posit that if drops with $D > 0.98$ mm were studied, their rotation characteristics would follow Eq.(5). However, drops such that $D/D_{\mathrm{T}} > 0.25$ would not follow Eq.(5) when large enough to be affected by shear at the core-sheath interface for $r_{\mathrm{U}} < 1$. Drops exceeding $D = 0.98 - 9.6$ mm would likely exhibit behavioral modes characterized by shape deformation and off-axis rotation due to a reduction in Laplace pressure, which are observed for large drops in high velocities in laminar flows[8]. The

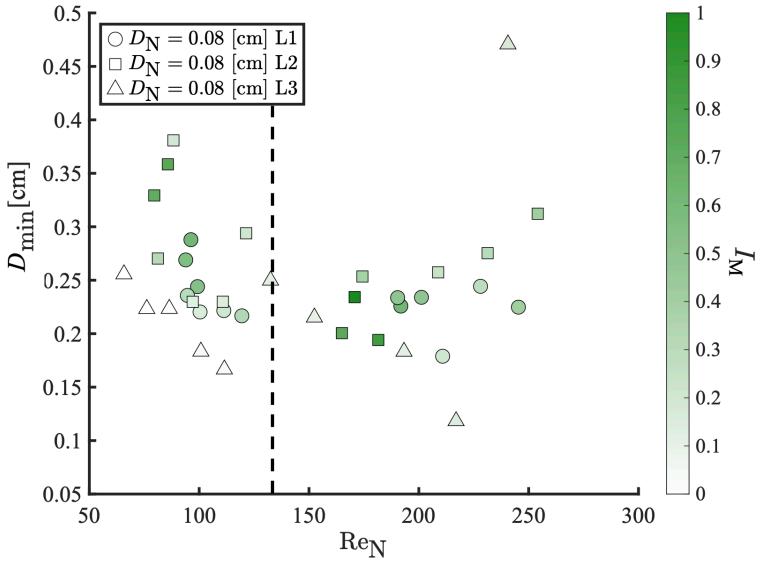


Figure 11: Turbulence intensity modulates the onset of drop rotation. The minimum drop size that will rotate at in flow, $D_{\min}$, is plotted against the needle Reynolds number with colors corresponding to turbulence intensity.

deviation from Eq.(5) that occurs as drop size approaches that of the tube diameter is a phenomena that we would expect to occur for other tube diameters, if tested. Though only one tube diameter is examined in this study, its impact upon rotation is evident by the change in St at large D/D_T. Likely, increasing or decreasing D_T would subsequently scale the value of D/D_T at which rotation deviates from Eq.(5).

In our previous work in laminar flows, we found that the size of the capillary support influences drop rotation; an affect we hypothesized was due to the obfuscation of vortical formation in the drop wake. We likewise investigated the influence of needle diameter to angular velocity in turbulent-shearing flows, but due to the increased number of experimental parameters we limited our investigation of the role of needle diameter to one fixture position at which we compared two needle diameters. We discovered at near the exit of the core flow, drops on larger needles rotate slower than drops on smaller needles; which is the opposite of what we observed in laminar flows. According to the force balance given in our previous work, the capillary force governs the highest rotational speed a drop can withstand before pinch-off occurs. Likewise, Eqs. (1) and (2) indicate that increasing D_T increases the allowable aerodynamic torque a drop can sustain prior to pinch-off in the lateral direction. Thus, the decrease in ω for increased D_N near L3 is surprising. We assert that this behavior is due to the increased magnitude of shear near the tube outlet. At locations with lower shear, such as L2 and L1 in **Fig.5**a-c, we expect that increasing D_N increases ω.

4.2 Sheathed coaxial jet-flow phenomena

The superposition of a co-flowing airstream and a jet creates our sheathed, coaxial jet-flow. While such a flow has not been yet coined as sheathed, coaxial jet-flow; other fluid systems have made use of the phenomena surrounding the superposition of a jet and a co-flowing airstream. Propulsion systems, such as missiles and turbine engines possess, and exhausting systems, such as car exhausts or fume stacks, both exhaust jets into a co-flowing airstream. Propulsion systems are characterized by $r_U \gg 1$ as the jet-exhaust velocity is significantly higher than any freestream velocity[23] Automobile engine exhaust of a car in motion operates at varying r_U; where car speed and headwind form U_S. The presence of sheathed coaxial jet-flow across multiple systems merits it characterization in this study and future ones.

Sheathed coaxial jet-flow phenomena is characterized by U_S and r_U. For $r_U < 1$, the velocity field is similar to a jet flow emptying into ambient conditions where the core jet velocity would be $U_C - U_S$. Similarly, for $r_U < 1$, the flow field is similar to that of an airflow passing a long cylinder where freestream velocity is $U_S - U_C$. Rather than simply studying these similar cases, we employ both the sheath and core flows to mitigate the turbulent instability that a jet emptying into ambient. The range of r_U examined for a fixed

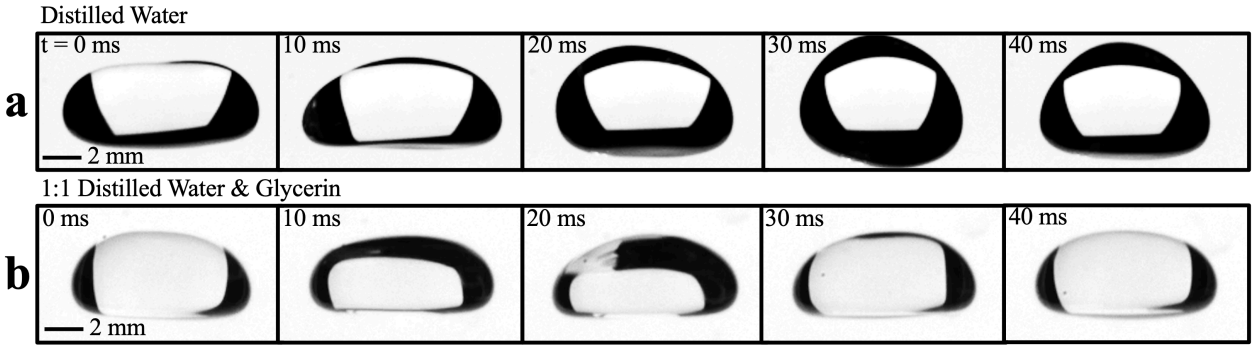


Figure 12: Drops of distilled water (**a**) and 1:1 distilled water and glycerin (**b**) are levitated in turbulent shearing flow created by sheathed, coaxial jet-flow.

U_S in this study was limited to $r_U = 0.2 - 1.4$. We posit that for $r_U < 0.2$, downstream turbulence would continue to increase with decreasing r_U, following the trend of **Fig.6**d. For $r_U > 1.4$, local turbulence would likely increase following the trend of **Fig.6**d.

The wind tunnel used in this study was first used to observe the oscillation of pendant drops in laminar flows[8]. Upon modification, it now has been used to create turbulent-shearing flows and record drop motion within. In addition to studying pendant drops, our wind tunnel can been used to levitate liquid drops, as shown in **Fig.12**. Shear at the core-sheath interface for $r_U < 1$ and large U_S creates a downstream region where drop levitation in turbulent-shearing flow is possible for many minutes. At this stable region, the drop levitates above the core airflow and aerodynamic shear prohibits the drop from entering the sheath. We form a pendant drop near L1 above the core and allow the drop to pinch-off, then the drop falls slightly and levitation ensues. Changing the value of r_U allows us to create various levels of turbulence in the flow as well as account for changes in drop size due to evaporation. Employing the pendant drop system used to pinch-off the first levitating drop, we have the ability to inject sequential drops of varying liquids to film their interactions, including coalescence. Such capacities enable the study of liquid mixing in air, quasi-contactless rheology, drops with surface active species, and drops undergoing chemical reactions in which drop oscillation modulates kinetics.

5 Conclusion

We subject pendant drops to vertical, turbulent, and shearing flows and report their dynamics or lack thereof. Turbulence mutes pendant drop dynamics. The turbulent, shearing flow field is provided by a sheathed, coaxial jet in a vertical wind tunnel, a novel flow field that is similar to a coaxial jet. By exhausting a core jet into a suction-type vertical wind tunnel, we subject pendant drops to various magnitudes of nonuniform disturbances arising from turbulence and shear. We employ an Eulerian-based finite-volume CFD solver within Star-CCM to provide flow characterizations from which to visualize sheathed, coaxial jet flow and understand pendant drop dynamics therein. The amount of turbulence and shear downstream of the core jet is governed by the velocity ratio, the sheath flow velocity, and the downstream distance from the core jet exit. Pendant drops that rotate in the presence of ascending, turbulent, and shearing flow circumvent the needle support on either a fixed plane (the (1a,0) mode) or experience vertical migration of the centroid (the (1b,0) mode). Generally, rotating drops exhibit mode (1a,0), but in regions of increased shear and turbulence mode (1b,0) is prevalent. Contrary to pendant drop dynamics in laminar flows, modes where drops exhibit periodic shape deformations are not prevalent.

Rotating pendant drops do so at speeds between $50-300$ rad/s in turbulent, shearing flows. Drop rotation is influenced by the needle diameter, the velocity ratio between the core and sheath, and the average velocity, turbulence intensity, and shear imposed on the drop. As the drop Reynolds number increases, the drop angular velocity decreases. Similarly, smaller drops rotate faster than larger drops. Drops adhered to small needles rotate faster than those adhered to large needles, the inverse of the observed behavior of pendant drops in laminar flows. Reynolds number becomes a better metric by which to characterize drop angular

velocity as the magnitudes of turbulence increase. Turbulence simplifies drop rotation to be primarily a function of Reynolds number. Reynolds number effectively characterizes dimensionless drop rotation, given by a modified Strouhal number, and negatively correlates with Strouhal number. The Reynolds number fails to characterize dimensionless rotation for two outlying data sets represented by subsets of drop sizes for velocity ratios less than unity at the two locations farthest away from the core outlet. By examining the energetics of a rotating pendant drop, the Strouhal number is shown to scale according to an inverse Reynolds number with $R^2 = 0.95$. When dimensionless drop rotation deviates from the scaling law, we find that the drop nears the flow interface above the tube wall. At that interface, increased levels of shear deviate dimensionless rotation from the general trend. Across both laminar and turbulent conditions, the scaling law effectively describes the relationship between drop inertia and dimensionless rotation with $R^2 = 0.91$. Therefore, the onset of turbulence does not greatly augment the dimensionless rotation of pendant drops compared to laminar flows. However, the onset of rotation greatly influences the minimum drop size that will rotate at each flow condition below a threshold needle Reynolds number. Below the threshold, turbulence increases the minimum drop size that will rotate at a given flow condition.

References

[1] A. Aalilija, Ch.-A. Gandin, and E. Hachem. On the analytical and numerical simulation of an oscillating drop in zero-gravity. *Computers & Fluids*, 197:104362, 2020. ISSN 0045-7930. doi: https://doi.org/10.1016/j.compfluid.2019.104362. URL `https://www.sciencedirect.com/science/article/pii/S0045793019303214`.

[2] I. Angelin, R. Naren Shankar, K. Sathish Kumar, K. Anusindhiya, K. Vijayaraja, and E. Rathakrishnan. Characterization of lip thickness effects in subsonic coaxial jets with varying velocity ratio. *Journal of applied fluid mechanics*, 18(10):2518–2534, 2025. ISSN 1735-3572.

[3] H. Au and N.W.M. Ko. Coaxial jets of different mean velocity ratios, part 2. *Journal of Sound and Vibration*, 116(3):427–443, 1987. ISSN 0022-460X. doi: https://doi.org/10.1016/S0022-460X(87)81375-5. URL `https://www.sciencedirect.com/science/article/pii/S0022460X87813755`.

[4] Osman A. Basaran and David W. DePaoli. Nonlinear oscillations of pendant drops. *Physics of Fluids*, 6(9):2923–2943, 09 1994. ISSN 1070-6631. doi: 10.1063/1.868120. URL `https://doi.org/10.1063/1.868120`.

[5] G. K. Batchelor and I. Proudman. The effect of rapid distortion of a fluid in turbulent motion. *The Quarterly Journal of Mechanics and Applied Mathematics*, 7(1):83–103, 1954.

[6] A. Bussonnière, M. Baudoin, P. Brunet, and O. Bou Matar. Dynamics of sessile and pendant drops excited by surface acoustic waves: Gravity effects and correlation between oscillatory and translational motions. *Phys. Rev. E*, 93:053106, May 2016. doi: 10.1103/PhysRevE.93.053106. URL `https://link.aps.org/doi/10.1103/PhysRevE.93.053106`.

[7] CHRISTOPHE CLANET and JUAN C. LASHERAS. Transition from dripping to jetting. *Journal of Fluid Mechanics*, 383:307–326, 1999. doi: 10.1017/S0022112098004066.

[8] Jacob D Dockery, Duygu Yilmaz Aydin, and Andrew K Dickerson. Pendant drop motion and stability in vertical airflow. *Physics of Fluids*, 36(2), 2024.

[9] H. L. Dryden and G. B. Schubauer. The use of damping screens for the reduction of wind-tunnel turbulence. *Journal of the Aeronautical Sciences*, 14(4):221–228, 1947.

[10] C. Emersic and P. J. Connolly. The breakup of levitating water drops observed with a high speed camera. *Atmospheric Chemistry and Physics*, 11(19):10205–10218, October 2011. ISSN 1680-7316. doi: 10.5194/acp-11-10205-2011. URL `https://acp.copernicus.org/articles/11/10205/2011/`.

[11] C. Ferrera, J. M. López-Herrera, M. A. Herrada, J. M. Montanero, and A. J. Acero. Dynamical behavior of electrified pendant drops. *Physics of Fluids*, 25(1):012104, 01 2013. ISSN 1070-6631. doi: 10.1063/1.4776238. URL `https://doi.org/10.1063/1.4776238`.

[12] S. Gavrilakis. Numerical simulation of low-reynolds-number turbulent flow through a straight square duct. *Journal of Fluid Mechanics*, 244:101–129, 1992.

[13] R. Govardhan and C.H.K. Williamson. Vortex-induced motions of a tethered sphere. *Journal of Wind Engineering and Industrial Aerodynamics*, 69-71:375–385, 1997. ISSN 0167-6105. doi: https://doi.org/10.1016/S0167-6105(97)00170-0. URL https://www.sciencedirect.com/science/article/pii/S0167610597001700. Proceedings of the 3rd International Colloqium on Bluff Body Aerodynamics and Applications.

[14] Omid Mosalman Haghighi, Ghasem Zargar, Abbas Khaksar Manshad, Muhammad Ali, Mohammad Ali Takassi, Jagar A. Ali, and Alireza Keshavarz. Effect of environment-friendly non-ionic surfactant on interfacial tension reduction and wettability alteration; implications for enhanced oil recovery. *Energies*, 13(15), 2020. ISSN 1996-1073. doi: 10.3390/en13153988. URL https://www.mdpi.com/1996-1073/13/15/3988.

[15] D.M. Henderson, W.G. Pritchard, and L.B. Smolka. On the pinch-off of a pendant drop of viscous fluid. *Physics of Fluids*, 9:3188, 1997.

[16] Holger Homann, Jérémie Bec, and Rainer Grauer. Effect of turbulent fluctuations on the drag and lift forces on a towed sphere and its boundary layer. *Journal of Fluid Mechanics*, 721:155–179, April 2013. ISSN 0022-1120, 1469-7645. doi: 10.1017/jfm.2013.66. URL https://www.cambridge.org/core/product/identifier/S0022112013000669/type/journal_article.

[17] Madhuvanthi A Kandadai, Praveena Mohan, Genyao Lin, Anthony Butterfield, Mikhail Skliar, and Jules J Magda. Comparison of surfactants used to prepare aqueous perfluoropentane emulsions for pharmaceutical applications. *Langmuir*, 26(7):4655–4660, 2010.

[18] Jesse D. Killion and Srinivas Garimella. Simulation of pendant droplets and falling films in horizontal tube absorbers. *Journal of Heat Transfer*, 126(6):1003–1013, 01 2005. ISSN 0022-1481. doi: 10.1115/1.1833364. URL https://doi.org/10.1115/1.1833364.

[19] A.S.H. Kwan and N.W.M. Ko. Coherent structures in subsonic coaxial jets. *Journal of sound and vibration*, 48(2):203–219, 1976. ISSN 0022-460X.

[20] Mohd Talib Latif and Peter Brimblecombe. Surfactants in atmospheric aerosols. *Environmental Science & Technology*, 38(24):6501–6506, 2004. doi: 10.1021/es049109n. URL https://doi.org/10.1021/es049109n. PMID: 15669305.

[21] Jongwon Lee and Wontae Hwang. Equilibrium shapes and dynamics of pendant drops within a uniform vertical flow. *Journal of Fluid Mechanics*, 1020:A42, 2025.

[22] R. I. Loehrke and H. M. Nagib. Control of free-stream turbulence by means of honeycombs: a balance between suppression and generation. *Journal of Fluids Engineering*, 98(3):342–353, 1976.

[23] Jack D. Mattingly, Keith M. Boyer, and Hans von Ohain. Elements of propulsion : gas turbines and rockets, 2016.

[24] F. R. Menter. Two-equation eddy-viscosity turbulence models for engineering applications. *AIAA Journal*, 32(8):1598–1605, 1994.

[25] Jong Hoon Moon, Byung Ha Kang, and Ho-Young Kim. The lowest oscillation mode of a pendant drop. *Physics of fluids*, 18(2), 2006.

[26] Ziqing Pan, JP Martin Trusler, Zhijun Jin, and Kaiqiang Zhang. Interfacial property determination from dynamic pendant-drop characterizations. *Nature protocols*, 20(2):363–386, 2025.

[27] Lauren M. Parkinson and Chi M. Phan. Natural vibration of an aqueous pendant drop. *Experimental Thermal and Fluid Science*, 90:48 – 54, 2018. ISSN 0894-1777. doi: https://doi.org/10.1016/j.expthermflusci.2017.09.003. URL http://www.sciencedirect.com/science/article/pii/S0894177717302674.

[28] S. V. Patankar and D. B. Spalding. A calculation procedure for heat, mass and momentum transfer in three-dimensional parabolic flows. *International Journal of Heat and Mass Transfer*, 15(10):1787–1806, 1972.

[29] L. Prandtl. Attaining a steady air stream in wind tunnels. Technical Report TM-726, NACA, 1933.

[30] I. Rodriguez, O. Lehmkuhl, and M. Soria. On the effects of the free-stream turbulence on the heat transfer from a sphere. *International Journal of Heat and Mass Transfer*, 164:120579, January 2021. ISSN 00179310. doi: 10.1016/j.ijheatmasstransfer.2020.120579. URL https://linkinghub.elsevier.com/retrieve/pii/S0017931020335158.

[31] I. Rodríguez, O. Lehmkuhl, R. Borrell, and A. Oliva. Flow dynamics in the turbulent wake of a sphere at sub-critical Reynolds numbers. *Computers & Fluids*, 80:233–243, July 2013. ISSN 00457930. doi: 10.1016/j.compfluid.2012.03.009. URL https://linkinghub.elsevier.com/retrieve/pii/S0045793012000965.

[32] Alexandre Schmit, Laurent Courbin, Mélanie Marquis, Denis Renard, and Pascal Panizza. A pendant drop method for the production of calibrated double emulsions and emulsion gels. *Rsc Advances*, 4(54): 28504–28510, 2014.

[33] Nathan B. Speirs, Jesse L. Belden, and Aren M. Hellum. The capture of airborne particulates by rain. *Journal of Fluid Mechanics*, 958:A40, 2023. doi: 10.1017/jfm.2023.101.

[34] Miklos Szakall, Karoline Diehl, Subir K Mitra, and Stephan Borrmann. A wind tunnel study on the shape, oscillation, and internal circulation of large raindrops with sizes between 2.5 and 7.5 mm. *Journal of the Atmospheric Sciences*, 66(3):755–765, 2009.

[35] Miklos Szakall, Subir K Mitra, Karoline Diehl, and Stephan Borrmann. Shapes and oscillations of falling raindrops—a review. *Atmospheric Research*, 97(4):416–425, 2010.

[36] Nilofar Taraki and A. Said Ismail. Focused liquid pinching in coaxial drop capsule generation. *Langmuir*, 42(8):6344–6353, 2026. doi: 10.1021/acs.langmuir.5c06135. URL https://doi.org/10.1021/acs.langmuir.5c06135. PMID: 41708294.

[37] F. Y. Testik, A. P. Barros, and L. F. Bliven. Toward a physical characterization of raindrop collision outcome regimes. *Journal of the Atmospheric Sciences*, 68(5):1097–1113, April 2011. ISSN 0022-4928, 1520-0469. doi: 10.1175/2010JAS3706.1. URL https://journals.ametsoc.org/view/journals/atsc/68/5/2010jas3706.1.xml.

[38] René van Hout, Sudharson Murugan, Abhijit Mitra, and Beni Cukurel. Coaxial circular jets—a review. *Fluids*, 6(4), 2021. ISSN 2311-5521. doi: 10.3390/fluids6040147. URL https://www.mdpi.com/2311-5521/6/4/147.

[39] E. VILLERMAUX and H. REHAB. Mixing in coaxial jets. *Journal of Fluid Mechanics*, 425:161–185, 2000. doi: 10.1017/S002211200000210X.

[40] Herman Wijshoff. Drop dynamics in the inkjet printing process. *Current opinion in colloid & interface science*, 36:20–27, 2018.

[41] Edward D. Wilkes and Osman A. Basaran. Drop ejection from an oscillating rod. *Journal of Colloid and Interface Science*, 242(1):180–201, 2001. ISSN 0021-9797. doi: https://doi.org/10.1006/jcis.2001.7729. URL https://www.sciencedirect.com/science/article/pii/S002197970197729X.

[42] C.H.K. Williamson and R. Govardhan. Dynamics and forcing of a tethered sphere in a fluid flow. *Journal of Fluids and Structures*, 11(3):293–305, 1997. ISSN 0889-9746. doi: https://doi.org/10.1006/jfls.1996.0078. URL https://www.sciencedirect.com/science/article/pii/S088997469690078X.

[43] Geoff R. Willmott, Chiara Neto, and Shaun C. Hendy. Uptake of water droplets by non-wetting capillaries. *Soft Matter*, 7:2357–2363, 2011. doi: 10.1039/C0SM00574F. URL http://dx.doi.org/10.1039/C0SM00574F.

[44] Yufei Xie, Hao Chen, Tao An, Yihan Wang, and Haisheng Fang. Pinch-off dynamics of the dripping mode under an axial electric field. *Langmuir*, 41(30):20328–20342, 2025. doi: 10.1021/acs.langmuir.5c02712. URL https://doi.org/10.1021/acs.langmuir.5c02712. PMID: 40702673.

[45] Junyi Yang, Nikoo Moradpour, Lap Au-Yeung, and Peichun Amy Tsai. Lab-on-a-chip insights: advancing subsurface flow applications in carbon management and hydrogen storage. *Lab Chip*, 26:1352–1393, 2026. doi: 10.1039/D5LC00428D. URL http://dx.doi.org/10.1039/D5LC00428D.

[46] Fei Zhang and Xinping Zhou. Static and dynamic stability of pendant drops. *Journal of Fluid Mechanics*, 968:A30, 2023.

[47] Hepeng Zheng, Yun Zhang, Haoran Li, Zuhang Wu, Yanqiong Xie, and Lifeng Zhang. Raindrop deformation in turbulence. *Geophysical Research Letters*, 51(9):e2024GL108627, 2024. doi: https://doi.org/10.1029/2024GL108627. URL https://agupubs.onlinelibrary.wiley.com/doi/abs/10.1029/2024GL108627. e2024GL108627 2024GL108627.

Supplementary Files

This is a list of supplementary files associated with this preprint. Click to download.

- PendantDropDynamicsinSheathFlows.pdf